

Article

# Effect of Bonding Temperature on Crack Occurrences in Al<sub>2</sub>O<sub>3</sub>/SS 430 Joints Using Cu-Based Brazing Alloys

Hoejun Heo <sup>1</sup>, Gyulin Kim <sup>1</sup>, Yoon-Cheol Park <sup>2</sup>, Keeyoung Jung <sup>2,\*</sup>  and Chung-Yun Kang <sup>1,\*</sup>

<sup>1</sup> Department of Materials Science and Engineering, Pusan National University (PNU), Pusan 46241, Korea; hjheo@pusan.ac.kr (H.H.); gyulin\_k@pusan.ac.kr (G.K.)

<sup>2</sup> Materials Research Division, Research Institute of Industrial Science and Technology (RIST), Pohang 37673, Korea; oohaha74@rist.re.kr

\* Correspondence: keeyoung.jung@rist.re.kr (K.J.); kangcy@pusan.ac.kr (C.-Y.K.); Tel.: +82-10-5440-1011 (K.J.); +82-10-8329-8429 (C.-Y.K.)

Received: 3 September 2018; Accepted: 20 September 2018; Published: 23 September 2018



**Abstract:** The effect of bonding temperature on crack occurrences in  $\alpha$ -Al<sub>2</sub>O<sub>3</sub>/SS 430 joints using Cu-based brazing alloys was investigated with emphasis on the microstructural characterization, hardness, and analytical residual stresses of the joints. The brazing was conducted using Cu-7Al- $x$ Ti and Cu-7Al- $x$ Zr ( $x = 2.5, 3.5,$  and  $4.5$ ) alloys at 1000 °C and 1080 °C leading to solid-liquid and liquid-state bonding, respectively. Cracks occurred in the joints brazed at 1080 °C irrespective of the alloys, while crack-free joints were obtained at 1000 °C for joints with only Cu-7Al- $x$ Zr alloys. Increases in the bonding temperature or utilization of Cu-7Al- $x$ Ti alloys led to a formation of brittle Fe-containing intermetallic or Fe-Cr phases in the brazed seams due to the dissolution of Fe from SS 430, which deteriorated the mechanical properties of the brazed seam. Maximum residual stresses of the real brazed joint were obtained by combining the calculated yield strength and measured hardness of the brazed seams. Eventually, when the hardness of the brazed seam was less than 107 Hv, the yield strength was 124 MPa or less and the maximum residual stress generated in the joint corresponded to 624 MPa or less, leading to a crack-free joint.

**Keywords:** ceramic-metal joining; brazing; residual stress; edge crack; hardness; microstructure

## 1. Introduction

Active brazing alloys (ABA) have been widely used for brazing between metal/ceramic or ceramic/ceramic couples in various industrial applications. Brazed joints with the alloys utilize a simple process and exhibit high bonding strength (49–325 MPa) and good oxidation resistance ( $10^{-10}$ – $10^{-12}$  g<sup>2</sup> cm<sup>-4</sup> s<sup>-1</sup> at 400–600 °C) at high temperatures of up to 500 °C [1–4], and thus it is reasonable to consider ABA as a sealing material for the heterogeneous joints in sodium beta-alumina batteries (NBBs) that operate in the temperature range of 280–350 °C and are exposed to liquid sodium (Na) [5–10]. The requirements for the use of an active brazing alloy in Na batteries includes high-temperature stability, sufficient bonding strength with Al<sub>2</sub>O<sub>3</sub>, and good corrosion resistance to liquid Na. Typical active brazing alloys, such as Ag-Cu-Ti and Cu-Al-Si-Ti, exhibit high-melting temperatures of 780–910 °C and 1001–1024 °C, respectively, and provide good bonding strength [2,11]. However, the two alloys containing Ag and Si that are soluble in liquid Na at 350 °C such that they do not guarantee reliability in the Na batteries [6,7]. In order to develop advanced high-temperature ABAs, our previous study introduced Cu-based brazing alloys, namely Cu-7Al- $x$ Ti and Cu-7Al- $x$ Zr ( $x = 2.5, 3.5,$  and  $4.5$ ) [12]. In these alloys, Cu is a parent constituent element that determines the baseline of the brazing temperature, Al is added to adjust (typically lower) the liquidus temperatures of the alloys, and Ti and Zr aid in a highly chemical reaction by forming reaction products such as Ti-O and Zr-O

oxides [3,13–15]. The alloys were composed of non-reactive elements against liquid Na at 350 °C and 500 °C as determined by inspection of the Cu-Na [16], Al-Na [17], Ti-Na [18], and Zr-Na [19]. The solidus points for six alloys correspond to 965, 965, 965, 945, 945, and 933 °C, respectively, and the liquidus point for them are 1033, 1026, 1013, 1051, 1045, and 1025 °C, respectively. Although both alloys exhibit good stability against high temperatures and resistance to Na corrosion, a consecutive study has not been conducted.

In considering the application of the new ABAs for ceramic–metal joints, preventing crack occurrence caused by the residual stress, which is due to the mismatch in the coefficient of thermal expansion (CTE), is important to obtain a high bonding strength [20–25]. In order to relieve the residual stress of the joint, a layer with a low yield strength and a high plastic deformation ability was previously reported, and ceramic particles such as tungsten carbide (WC) were added to the brazing alloy to reduce the CTE differences with ceramic [25–27]. However, previous studies only considered Si<sub>3</sub>N<sub>4</sub> ceramics and did not examine liquid Na corrosion resistance. Hence, this is insufficient for application to ceramic–metal joints in NaS cells.

In the study, it is considered using a lower bonding temperature between liquidus and solidus temperatures of the brazing alloy, solid–liquid-state bonding, to prevent crack occurrence in the  $\alpha$ -Al<sub>2</sub>O<sub>3</sub>/SS 430 joint. Commercial brazing processes are conducted at the aforementioned melting temperature of the brazing alloy since liquid-state bonding and a high temperature process accelerates the growth of reaction layers at the interface and formation of brittle intermetallic compounds, which are formed by the dissolution of base metal substrates into the brazing alloy [28,29]. However, the solid–liquid state bonding is expected to prevent dissolution of the base metal since the solubility of Fe from steel into the braze decreases with lower temperature. Additionally, with respect to the decreased intermetallic compounds, it is helpful to decrease the hardness and brittleness of the brazed seam by preventing cracking at the joint [27]. In addition, it is considered that solid–liquid state bonding reduces the shrinkage stress of the brazing alloys with partial liquids during cooling [30]. Therefore, in this study, the effect of bonding temperature on the crack occurrence in  $\alpha$ -Al<sub>2</sub>O<sub>3</sub>/SS 430 brazed joints using Cu-based alloys was investigated with emphasis on their microstructural characterization, hardness, and numerical residual stresses.

## 2. Materials and Methods

An  $\alpha$ -Al<sub>2</sub>O<sub>3</sub> ceramic (97% pure, 10  $\Phi$   $\times$  5 mm, Ujuoo Co., Busan, South Korea) and stainless steel (SS) 430 plate (Fe-14Cr-0.12C-1Mn-1Si, 12  $\times$  12  $\times$  3 mm<sup>3</sup>, Dongwon Special Steel Co., Busan, South Korea) was used as the base substrate. Ferritic SS 430 was selected since its CTE is smaller than that of austenitic SS 304 (Fe-10Ni-18Cr-0.08C-2Mn-1Si), and this aided in relieving the residual stress by decreasing the CTE mismatch with  $\alpha$ -Al<sub>2</sub>O<sub>3</sub>. The base materials were ground by #1200 SiC paper and then ultrasonically cleaned for 5 min prior to the brazing.

Two Cu-based brazing alloys, namely Cu-7Al-*x*Ti and Cu-7Al-*x*Zr (*x* = 2.5, 3.5, and 4.5), were fabricated via high-frequency induction casting using Cu (99.99%), Al (99.99%), Cu-5% Ti, and Cu-5% Zr alloys (Dongjin Metal Co., Busan, South Korea). The casting furnace was purged with Ar gas to reduce oxygen pressure after pumping to a low vacuum level of 10<sup>−2</sup> Torr. The alloys were poured into a rod-shaped mold with a diameter of 2.54 mm and solidified at room temperature. The alloys were then cut into 10 mm  $\times$  0.4 mm sections via electronic wire cutting, ground by #1200 down to a thickness of 0.2 mm, and then ultrasonically cleaned for 5 min. The melting points of the alloys were determined via a differential scanning calorimeter (DSC, Universal V4.5A, TA Instruments, New Castle, DE, USA) as 965–1033 °C and 933–1051 °C. The microstructures of the alloys were identified after immersing the alloy samples into an etchant solution of 1 g FeCl<sub>3</sub> + 1 mL HCl + 200 mL distilled water. The phases of the alloys were identified via optical microscopy (OM, BX-51M, Olympus, Tokyo, Japan), scanning electron microscopy (SEM, SUPRA45, Carl Zeiss, Oberkochen, Germany), energy diffraction X-ray (EDX), and X-ray diffraction (XRD, Ultima IV, Rigaku, Tokyo, Japan).

The prepared brazing alloys were placed between  $\text{Al}_2\text{O}_3$  and SS 430 base materials with 150 g loads on the  $\text{Al}_2\text{O}_3$  base material as shown in Figure 1. The specimens were placed in a vacuum furnace at a high vacuum of  $1.0 \times 10^{-5}$  Torr and heated to 1000 °C or 1080 °C at a heating rate of 10 °C/min. The specimens dwelled at the chosen temperature for 10 min, were cooled down at a rate of 2 °C/min. At the dwelling temperatures of 1000 °C and 1080 °C, a pressure of 2.00 g mm<sup>-2</sup> and 0.32 g mm<sup>-2</sup> was applied, respectively, perpendicular to the bonding plane to fix the brazing alloy.

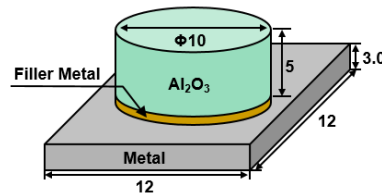


**Figure 1.** Schematic illustration of the brazed specimen.

The bonded specimens were cut perpendicular to the bonding area and the crack occurrence was examined via OM. The microstructures of the brazed seams were etched by the aforementioned solution, and the microstructures were identified using OM, SEM, EDX, and XRD analyses. With respect to the specimens for XRD, the as-brazed specimens were ground from the SS 430 side parallel to the bonded plane until the ground plane reached the center of the brazed seam.

### 3. Results and Discussion

#### 3.1. Crack Occurrence for the Brazed Joint

Figure 2 shows a cross-sectional optical microstructure (OM) of  $\alpha$ - $\text{Al}_2\text{O}_3$ /SS 430 joints bonded with Cu-7Al-3.5Ti and Cu-7Al-3.5Zr alloys at 1000 °C and 1080 °C via the solid–liquid- and liquid-state bonding, respectively. Cracks occur at the center and edges of the joints as indicated by the white arrows in the figures. Table 1 shows the crack occurrence of the joints with respect to the brazing alloys and bonding temperature. The specimens bonded at 1080 °C exhibited crack occurrences at the center and edges irrespective of the brazing alloys. However, in the case of specimens bonded at 1000 °C using the solid–liquid-state bonding, cracks existed in the joint with Cu-7Al- $x$ Ti alloys while cracks were not observed for the specimens with Cu-7Al- $x$ Zr alloys. The results indicated that a crack-free joint was obtained by using Cu-7Al- $x$ Zr ( $x = 2.5, 3.5, \text{ and } 4.5$ ) alloys at 1000 °C with solid–liquid-state bonding. Therefore, the specimens using Cu-7Al- $x$ Ti alloys were more susceptible to crack occurrence than specimens with Cu-7Al- $x$ Zr alloys.

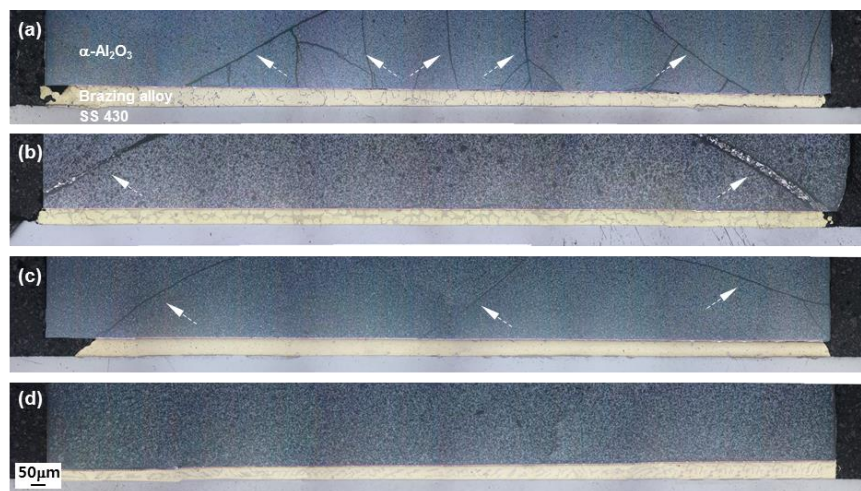


**Figure 2.** Optical microscopy (OM) of the joints for crack occurrence:  $\alpha$ -Al<sub>2</sub>O<sub>3</sub>/Cu-7Al-3.5Ti/SS 430 brazed at (a) 1080 °C and (b) at 1000 °C, and  $\alpha$ -Al<sub>2</sub>O<sub>3</sub>/Cu-7Al-3.5Zr/SS 430 brazed at (c) 1080 °C and (d) 1000 °C.

**Table 1.** Crack observation of the joints brazed with Cu-7Al-*x*Ti and Cu-7Al-*x*Zr (*x* = 2.5, 3.5, and 4.5) brazing alloys at 1080 °C and 1000 °C with the liquid- and solid-liquid-state bonding, respectively.

Bonding Temperature (°C)	Cu-7Al- <i>x</i> Ti (wt%)			Cu-7Al- <i>x</i> Zr (wt%)		
	2.5	3.5	4.5	2.5	3.5	4.5
1080 °C (Liquid)	O	O	O	O	O	O
1000 °C (Solid-liquid)	O	O	O	X	X	X

### 3.2. Finite Element Analysis of Residual Stress in Joints

Extant studies indicate that edge cracks in the ceramic-metal joint are generated by the residual stress caused by CTE differences with the metal and ceramics and the magnitude and distribution of the residual stress in the joints are typically measured by using the finite element method (FEM) [8,10,20,22,31,32]. In order to calculate the magnitude and distribution of residual stress in the joints brazed with brazing alloys, which is a main factor in increasing the crack susceptibility, a three-dimensional (3-D) FEM was used. Figure 3 shows the 3-D model shape of the  $\alpha$ -Al<sub>2</sub>O<sub>3</sub>/ABAs/SS 430 joint used in the FEM calculation, and Table 2 lists the elastic modulus (*E*), CTE, and Poisson's ratio of the base metal and brazing alloys, respectively, and the yield strength ( $\sigma_y$ ) and tangent coefficient (*G*) of brazing alloys at room temperature. The mechanical values (i.e., *E*,  $\sigma_y$ , and *G*) of brazing alloys were obtained via tensile tests with sub-size tensile specimens based on American Society for Testing and Materials (ASTM, West Conshohocken, PA, USA) E8/E8M-09 standards [33]. The thermal and physical property values (i.e., CTE and Poisson's ratio) of the brazing alloys were obtained by referring to compositionally similar Cu-7Al-2Fe alloy (C61400) [34]. The properties of  $\alpha$ -Al<sub>2</sub>O<sub>3</sub> and SS 430 are obtained in extant studies [35].

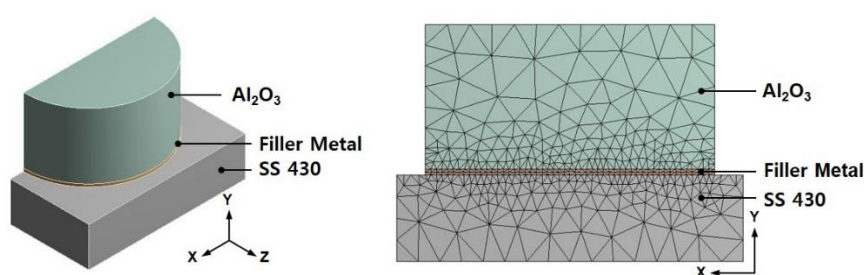


**Figure 3.** Finite element model of the symmetrical brazed specimen.

**Table 2.** Physical properties of the used materials for simulations (at 25 °C).

Materials	E (GPa) Elastic Mod.	$\sigma_y$ (MPa) Yield Str.	G(GPa) Tangent Mod.	$\alpha$ ( $10^{-6}/K$ ) CTE	Poisson's Ratio
Cu-7Al-2.5Ti	125 <sup>†</sup>	175 <sup>†</sup>	2.80 <sup>†</sup>		
Cu-7Al-3.5Ti	136 <sup>†</sup>	190 <sup>†</sup>	2.85 <sup>†</sup>		
Cu-7Al-4.5Ti	140 <sup>†</sup>	222 <sup>†</sup>	2.72 <sup>†</sup>		
Cu-7Al-2.5Zr	94 <sup>†</sup>	125 <sup>†</sup>	2.37 <sup>†</sup>	16.2 <sup>*</sup>	0.31 <sup>*</sup>
Cu-7Al-3.5Zr	96 <sup>†</sup>	133 <sup>†</sup>	2.28 <sup>†</sup>		
Cu-7Al-4.5Zr	98 <sup>†</sup>	145 <sup>†</sup>	2.13 <sup>†</sup>		
$\alpha$ -Al <sub>2</sub> O <sub>3</sub>	366 <sup>**</sup>	-	-	7.0 <sup>**</sup>	0.23 <sup>**</sup>
SS 430	200 <sup>**</sup>	-	-	10.4 <sup>**</sup>	0.24 <sup>**</sup>

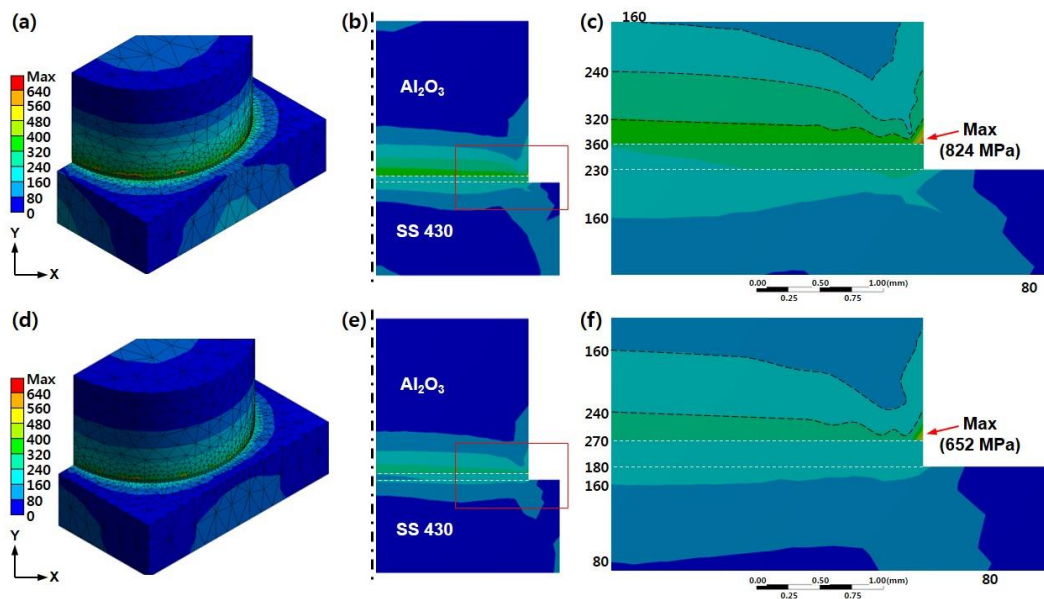
<sup>†</sup> Measured properties in tensile of a specimen based on the ASTM E8/E8M-09 standard. <sup>\*</sup> Copper and copper alloys, second ed., ASM international, 2001. <sup>\*\*</sup> Atlas of Stress-Strain Curves, second ed., ASM International, 2002.

The FEM software (ANSYS, ver. 15.0, ANSYS Inc., Canonsburg, PA, USA) was utilized to calculate the residual stress in the ceramic–metal joints. The 3-D cylindrical model with elastic–plastic behavior employed in the analysis is shown in Figure 3. The elements correspond to a triangle 6 node, and the mesh size was a normal mesh (600–1200  $\mu\text{m}$  interval). A fine mesh (60–200  $\mu\text{m}$  interval) was generated for the brazing alloys, Interface of the brazed substrate, and the total number of nodes and elements corresponded to 26,683 and 18,008, respectively. The boundary condition was set as a symmetry condition, and the base metal was fixed to prevent rigid body motion. The analytical conditions were assumed to correspond to gradual cooling from 1273 K below the solidus of brazing alloys to 300 K at room temperature and the joints were stress-free at the brazing temperature.

Figure 4 shows the von Mises stress distribution of  $\alpha$ -Al<sub>2</sub>O<sub>3</sub>/SS 430 brazed joints with Cu-7Al-3.5Ti (a–c) and Cu-7Al-3.5Zr (d–f) brazing alloys, and the maximum residual stresses of the joints are listed in Table 3. It is interesting that the calculated maximum residual stress was approximately 3–4 times higher than the yield strength of the brazing alloys (94–140 MPa) and tensile strength (350 MPa) of  $\alpha$ -Al<sub>2</sub>O<sub>3</sub>. Tensile stresses induced in the ceramic at the free surfaces of joined components can cause the propagation of flaws into the ceramic and the occurrence of “dome-shaped” edge crack in the joint since  $\alpha$ -Al<sub>2</sub>O<sub>3</sub> has a lower fracture toughness than that of Cu ( $\alpha$ -Al<sub>2</sub>O<sub>3</sub>:  $\approx$ 3.3–5, Cu: 12.3 MPa) [20–25]. In details for residual stresses, ceramics have significantly lower CTEs than metals (Al<sub>2</sub>O<sub>3</sub>: 8, ZrO<sub>2</sub>: 8, Al alloy: 21–24, Cu alloy:  $\approx$ 17–18, SS 304: 18, SS 430: 10.4 in  $10^{-6}$  K<sup>-1</sup> at 25 °C). For instance, on cooling a planar metal-ceramic component from a high-temperature to room-temperature at which bonding has been conducted, and where, to a first assumption, the component can be framed to be stress-free, the metal will wish to shrink more parallel to the interface than the ceramic. To maintain the joint, a complex stress state is applied at the interface called a residual stress or thermal stress [36,37]. It is noted that tensile stresses are induced in the ceramic at the free surfaces of bonded components and they considerably lower the fracture strength of joint material. These stresses can cause the propagation of cracks into the ceramic and the generation of edge cracks, occurring most of the ceramic from the metal and decrease the structural strength and increase the susceptibility of a joint to fatigue damage and fracture. Therefore, the residual stress in the joint due to the thermal expansion mismatch should be carefully considered when joining ceramic joining technologies with metal.

**Table 3.** Calculated maximum residual stress of the symbol  $\alpha$ -Al<sub>2</sub>O<sub>3</sub>/SS 430 joint with Cu-7Al-xTi and Cu-7Al-xZr (x = 2.5, 3.5, and 4.5) brazing alloys.

Brazing Alloys	Cu-7Al-xTi (wt%)			Cu-7Al-xZr (wt%)		
	2.5	3.5	4.5	2.5	3.5	4.5
Max residual stress (MPa)	750	824	872	620	652	674



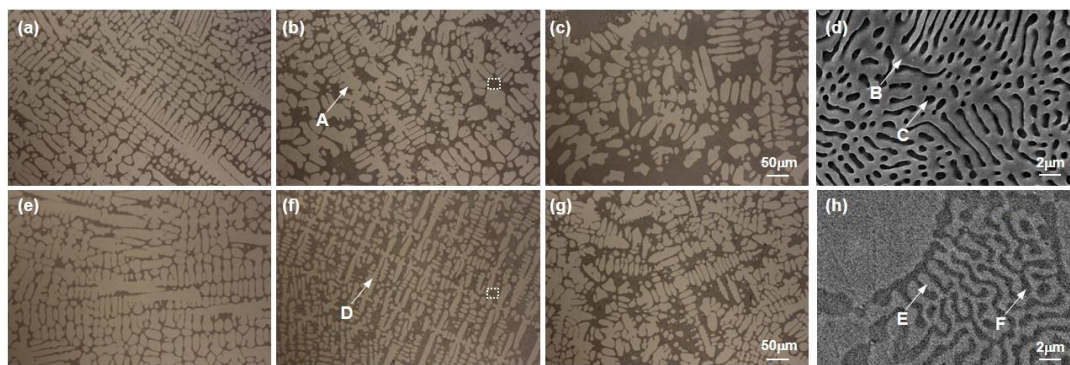
**Figure 4.** Von Mises stress distribution of  $\alpha$ -Al<sub>2</sub>O<sub>3</sub>/SS 430 joints brazed with (a–c) Cu-7Al-3.5Ti and (d–f) Cu-7Al-3.5Zr brazing alloys via the FEM method and their magnified views.

Figure 4b,c,e,f represent magnified areas of (a) and (d). The differences in the residual stress distribution of the brazed joints are summarized as follows: (1) The maximum residual stress was generated at the edge of the interface between the brazing alloys and Al<sub>2</sub>O<sub>3</sub> as indicated by the arrow in the figures. (2) The maximum residual stress in the Cu-7Al-x3.5Ti joint (at 824 MPa) exceeded that in Cu-7Al-3.5Zr (at 652 MPa). (3) The higher residual stress region occurred at the inner Al<sub>2</sub>O<sub>3</sub> from the bonding interface, and the region exceeding 160 MPa was wider in the Cu-7Al-3.5Ti joint (at 360–160 MPa) than that in the Cu-7Al-3.5Zr joint (270–160 MPa). (4) The residual stress inside the brazed seam was 230–360 MPa and 180–270 MP for the Cu-7Al-3.5Ti and Cu-7Al-3.5Zr joints, respectively, and the Cu-7Al-3.5Ti joint exhibited a higher stress distribution. It was concluded that the Cu-7Al-3.5Ti joint exhibited higher residual stress and a wider high-stress region when compared with those of the Cu-7Al-3.5Zr joint. In addition, it was observed that as the content of Ti and Zr in the brazing alloy increased, the maximum residual stress also increased. The discussion on the aforementioned relationship will be further studied in Section 3.4.

### 3.3. Microstructure and Hardness of the Bonded Interlayer

#### 3.3.1. Microstructure of Brazing Alloys

Figure 5 shows optical microscopy images of Cu-7Al-xTi (a–c) and Cu-7Al-xZr (e–g) brazing alloys and its magnified SEM images that are denoted as rectangular in (d) and (h). With respect to the six brazing alloys, dendritic shapes (white areas) and eutectic phases (black areas) along all the dendrite boundaries were observed. When the percentages of Ti or Zr of brazing alloys increased, the volume of eutectic phases also increased. Table 4 shows the results of EDX spot analysis of the distinctive phases labeled as A–F in Figure 5, and Figure 6 shows the XRD patterns of the alloys. The results indicate that the Cu-7Al-xTi alloys are composed of a primary  $\alpha$ -Cu solid solution (SS) containing approximately 12–13 at % Al (marked as A) and eutectic phases of alternating  $\alpha$ -Cu SS and AlCu<sub>2</sub>Ti intermetallic compounds. Similarly, the microstructure of the Cu-7Al-xZr alloys was composed of a primary  $\alpha$ -Cu SS (marked as D) and eutectic phase ( $\alpha$ -Cu + AlCu<sub>2</sub>Zr; marked as F). The second phases (AlCu<sub>2</sub>Ti and AlCu<sub>2</sub>Zr intermetallic compounds) were identified as face-centered-cubic (FCC) crystal structures similar to those in the  $\alpha$ -Cu solid solution.



**Figure 5.** Optical microscopy (OM) and SEM images (**d,h**) of the enlarged rectangular area in (**b**) and (**f**); (**a**) Cu-7Al-2.5Ti, (**b**) Cu-7Al-3.5Ti, (**c**) Cu-7Al-4.5Ti, (**e**) Cu-7Al-2.5Zr, (**f**) Cu-7Al-3.5Zr, and (**g**) Cu-7Al-4.5Zr.

**Table 4.** EDX spot analysis (at %) of the phases in Figure 5.

Label	Cu	Al	Ti	Zr	Possible Phase
A	87.9	12.1	-	-	$\alpha$ -Cu
B	87.7	12.3	-	-	$\alpha$ -Cu
C	51.3	25.9	24.2	-	AlCu <sub>2</sub> Ti
D	86.6	13.4	-	-	$\alpha$ -Cu
E	87.8	12.2	-	-	$\alpha$ -Cu
F	56.7	20.1	-	23.2	AlCu <sub>2</sub> Zr

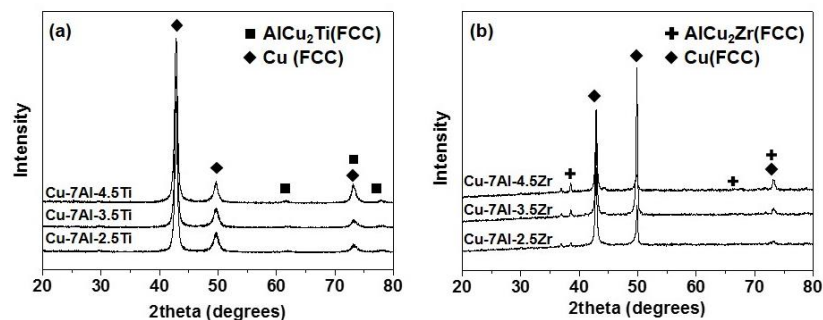


**Figure 6.** X-ray diffraction patterns of as-cast (**a**) Cu-7Al-*x*Ti and (**b**) Cu-7Al-*x*TZr brazing alloys.

### 3.3.2. Microstructure of the Brazed Seam in the Joint with Cu-7Al-*x*Ti

Figure 7 shows optical microscopy images of the joint bonded with three Cu-7Al-*x*Ti (*x* = 2.5, 3.5, and 4.5) brazing alloys at 1000 °C (a–c) and 1080 °C (e–g) along with the magnified SEM images (d,h) of areas denoted as rectangular. Table 5 lists the EDX point analysis for the six distinctive phases (T<sub>1</sub>–T<sub>6</sub>), and the XRD pattern of the center of the brazed seam parallel to the bonding plane is shown in Figure 8. The EDS and XRD analyses revealed that the primary  $\alpha$ -Cu SS (T<sub>1</sub>) and eutectic ( $\alpha$ -Cu + AlCu<sub>2</sub>Ti(T<sub>2</sub>)) phases similar to the microstructure in the aforementioned as-cast brazing alloys and fine AlCu<sub>2</sub>Ti (T<sub>3</sub>) form in the  $\alpha$ -Cu matrix in the brazed joint with Cu-7Al-*x*Ti brazing alloys processed at 1000 °C. When compared with the microstructure of the brazing alloys, it was found that the eutectic volume slightly decreased due to partially liquefied eutectics at 1000 °C since the solid–liquid temperature was used for forming reaction layers in the brazing process. Characterization of reaction layers is theoretically further discussed since it was determined that they were too thin to affect the residual stress of the brazed seam.

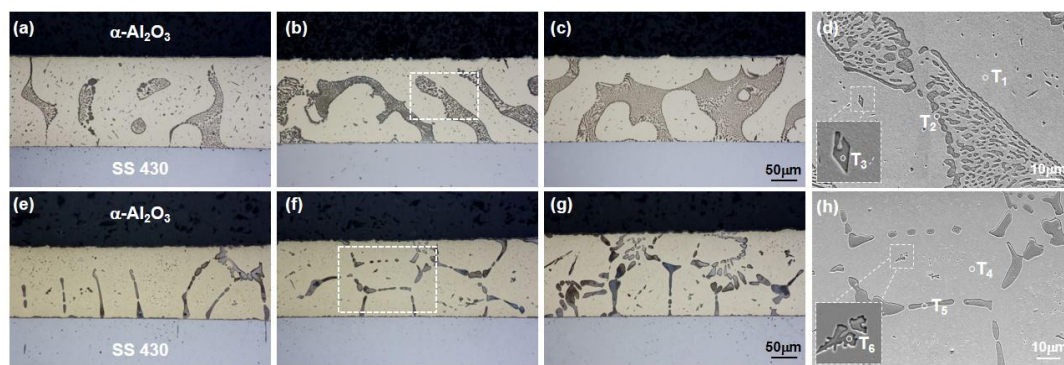


**Figure 7.** Optical microstructure (OM) of an  $\alpha$ -Al<sub>2</sub>O<sub>3</sub>/Cu-7Al-*x*Ti (*x* = 2.5, 3.5, and 4.5)/SS 430 joint brazed at 1000 °C (a–c) and 1080 °C (e–g) and its magnified SEM images (d,h).

**Table 5.** EDX analysis of the points in Figure 7 (at %).

Label	Cu	Al	Ti	Fe	Possible Phase
T <sub>1</sub>	88.0	12.0	-	-	$\alpha$ -Cu
T <sub>2</sub>	53.3	22.9	23.8	-	AlCu <sub>2</sub> Ti
T <sub>3</sub>	51.1	24.0	24.9	-	AlCu <sub>2</sub> Ti
T <sub>4</sub>	81.4	12.4	-	-	$\alpha$ -Cu
T <sub>5</sub>	39.4	25.1	25.1	10.1	AlCu <sub>2</sub> Ti(Fe)
T <sub>6</sub>	36.9	26.1	26.3	10.6	AlCu <sub>2</sub> Ti(Fe)

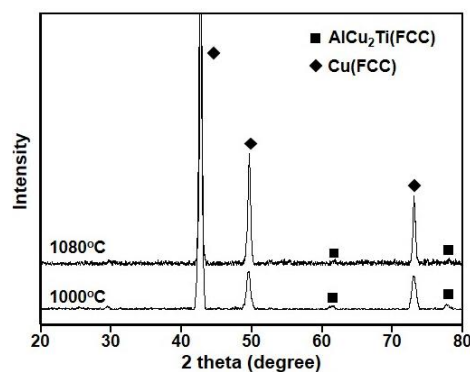


**Figure 8.** X-ray diffraction (XRD) patterns of the Cu-7Al-3.5Ti brazed seam bonded at 1080 °C and 1000 °C.

Conversely, the dendritic shape disappeared in the microstructure of the 1080 °C joint. A single-phase structure (T<sub>5</sub>) forms along the grain boundary of  $\alpha$ -Cu SS (T<sub>4</sub>), and a fine phase (T<sub>6</sub>) existed in the matrix. It should be noted that the AlCu<sub>2</sub>Ti phase contained 10–12 at % Fe, and this indicated the dissolution of Fe in SS 430 into the liquefied brazing alloy. Although the Fe-containing AlCu<sub>2</sub>Ti phase was identified to be AlCu<sub>2</sub>Ti through XRD as shown in Figure 8, it was termed AlCu<sub>2</sub>Ti(Fe) to avoid confusion in the study. In summary, the differences in microstructure based on the bonding temperature appeared in the morphology of the dendrite form (i.e., retention or disappearance) and composition of Fe in the second-phase AlCu<sub>2</sub>Ti.

Analysis of the diagram facilitated understanding of the phase formation as well as the cooling process. A phase diagram was used to further investigate phase formation between the brazing alloy (Cu-7.0Al-3.5Ti) and Fe from SS 430 at different bonding temperatures. Figure 9 shows a quasi-binary phase diagram of (Cu-7.0Al-3.5Ti)-*x*Fe (wt%) calculated via thermodynamic simulation software (Thermo-Calc ver. 3.1, Thermo-calc, Solna, Sweden). In the case of maintaining the bonding temperature of 1000 °C for solid–liquid-state bonding, the eutectic phases were partially liquefied as  $\alpha$ -Cu + L + eutectic ( $\alpha$ -Cu + AlCu<sub>2</sub>Ti), and the fine AlCu<sub>2</sub>Ti ( $\tau$ ) phase formed above 0.8 wt% Fe from the

partial liquid, thereby indicating that the  $\tau$  phase ( $T_3$ ) in  $\alpha$ -Cu SS formed during brazing. Conversely, when the brazing alloy was maintained at 1080 °C and completely existed in the liquid phase, while the  $\text{AlCu}_2\text{Ti}$  ( $\tau$ ) formed above 2.1 wt% Fe. Furthermore,  $\alpha$ -Cu SS was formed during the cooling process, and the residual liquid phase was transformed into a eutectic phase along the  $\alpha$ -Cu grain boundary. Thus, the  $\tau$  phase in the  $\alpha$ -Cu grain was formed during the holding stage at the brazing temperature, and the eutectic phase at the grain boundary was formed during the cooling stage. It was considered that the eutectic phase of the grain boundary, which corresponded to a single-phase form in contrast to the typical lamellar type, was formed using a degenerated eutectic reaction due to the small amount of residual liquid [38]. Furthermore, the  $\tau$  phase formation at 1080 °C appears to have corresponded to the Fe-containing  $\text{AlCu}_2\text{Ti}(\text{Fe})$  phase given that a high amount of Fe was diffused from the SS 430 interfaces.

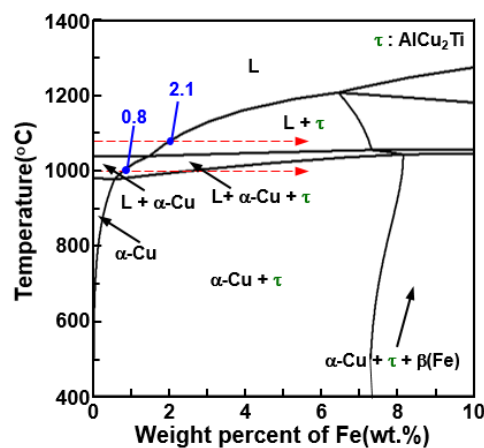
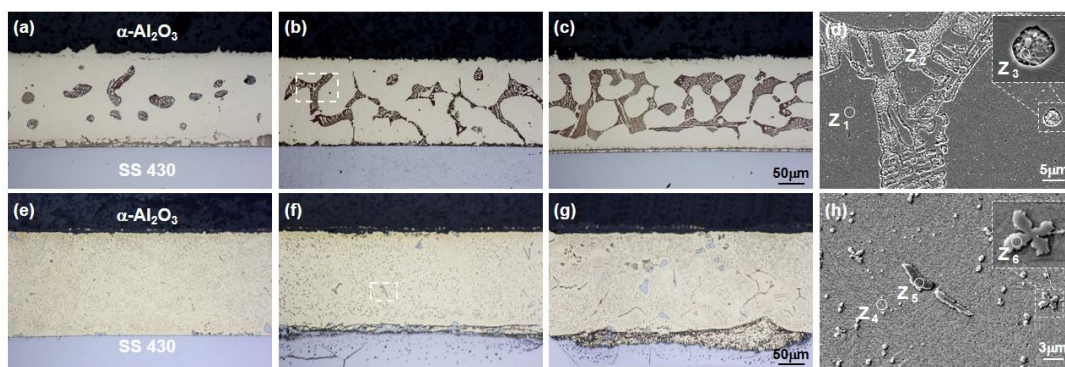


Figure 9. (Cu-7.0Al-3.5Ti)-xFe (wt%) quasi-binary phase diagram calculated via Thermo-calc software.

### 3.3.3. Microstructure of the Brazed Seam in the Joint with Cu-7Al-xZr

Figure 10 shows optical microscopy images of the joint bonded with three Cu-7Al-xTi ( $x = 2.5, 3.5, \text{ and } 4.5$ ) brazing alloys at 1000 °C (a–c) and 1080 °C (e–g) in conjunction with magnified SEM images (d,h) of the areas marked as rectangular. Table 6 shows the results of the EDX point analysis for the six distinctive phases ( $Z_1$ – $Z_6$ ). The XRD pattern of the center of brazed seam parallel to the bonding plane is shown in Figure 11. The EDS and XRD analyses confirmed that with respect to the brazed joint with Cu-7Al-xZr brazing alloys at 1000 °C, the primary  $\alpha$ -Cu SS ( $Z_1$ ) solid solution and eutectic ( $\alpha$ -Cu +  $\text{AlCu}_2\text{Zr}$  ( $Z_2$ )) phases were similar to the as-cast brazing alloys, and fine  $\text{AlCu}_2\text{Zr}$  ( $Z_3$ ) formed in the  $\alpha$ -Cu matrix. Conversely, the dendritic shape disappeared in the microstructure of the 1080 °C brazed joint, and fine phases ( $Z_5, Z_6$ ) form in  $\alpha$ -Cu ( $Z_4$ ). The fine phases mainly contained Fe, Cr, and small amounts of Al and Cu that were confirmed as body-centered cubic (BCC) crystal structures. It should be noted that the Zr element was not detected in the brazed seam. In order to track the existence of the Zr elements in the brazing alloys, Figure 12 shows the SEM micrograph (BSE mode) of the two interfaces of the  $\alpha$ - $\text{Al}_2\text{O}_3$ /Cu-7Al-3.5Zr/SS 430 joint brazed at 1080 °C. At the interface of  $\text{Al}_2\text{O}_3$ /Cu-7Al-3.5Zr, a 20–25  $\mu\text{m}$   $\text{ZrO}_2$  reaction layer (A) existed, and circular Cu particles (B) were distributed in the reaction layer. Fine Fe-Cr phases (C) and (D) existed in the brazed seam. Furthermore,  $\text{Al}_3\text{Fe}$  (E), which was formed by diffusing the Al in the brazing alloy into the SS 430, and  $\text{Zr}_2\text{Fe}$  (F) phases formed along the SS 430 interfaces. The aforementioned results indicate that the Zr elements of the brazing alloy were totally consumed for the formation of new phases by reacting with the base materials ( $\text{Al}_2\text{O}_3$ , SS 430) at the interface.



**Figure 10.** Optical microscopy of an  $\alpha$ -Al<sub>2</sub>O<sub>3</sub>/Cu-7Al-xZr ( $x = 2.5, 3.5, \text{ and } 4.5$ )/SS 430 joint brazed at 1000 °C (a–c) and 1080 °C (e–g) and its magnified SEM images (d,h).

**Table 6.** EDX analysis of the points in Figure 10 (at %).

Label	Cu	Al	Zr	Fe	Cr	Possible Phase
Z <sub>1</sub>	87.2	12.8	-	-	-	$\alpha$ -Cu
Z <sub>2</sub>	52.9	22.3	24.8	-	-	AlCu <sub>2</sub> Zr
Z <sub>3</sub>	54.7	22.4	22.9	-	-	AlCu <sub>2</sub> Zr
Z <sub>4</sub>	87.9	12.1	-	-	-	$\alpha$ -Cu
Z <sub>5</sub>	5.0	12.6	-	53.3	29.1	Fe-Cr
Z <sub>6</sub>	3.7	13.9	-	52.6	29.8	Fe-Cr

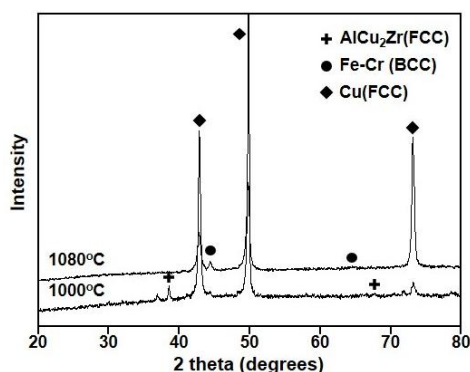


**Figure 11.** X-ray diffraction (XRD) patterns of the Cu-7Al-3.5Zr brazed interlayer bonded at 1080 °C and 1000 °C.

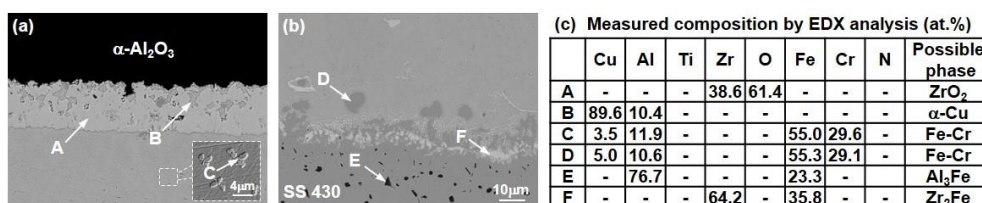


**Figure 12.** SEM images of each of the (a)  $\alpha$ -Al<sub>2</sub>O<sub>3</sub>/Cu-7Al-3.5Zr and (b) Cu-7Al-3.5Zr/SS 430 interfaces, respectively, along with (c) the measured composition for five distinct phases (A–E) obtained using EDX analysis (at %).

In order to understand the formation process of the Fe-Cr phases in the brazed seam, a phase diagram was calculated via the Thermo-Calc thermodynamic software. The average composition of the brazed seam (with the exception of Fe) was detected as Cu-6.4Al-0.6Cr via EDX mapping analysis. Figure 13 shows the (Cu-6.4Al-0.6Cr)-xFe quasi binary phase diagram by assuming that Fe was dissolved in the liquid brazing alloy. The Fe-Cr ( $\beta$ ) phase formed when Fe was dissolved above 2.8 wt% at 1080 °C. The formation is also reported in arc brazing of ferrite stainless steel by using

Cu-Al brazing alloy in which the steel is partially dissolved into the brazed seam to form the Fe-Cr phases [39]. It was concluded that Zr in the brazing alloy was used to form a reaction layer at the bonding interface, and Fe and Cr in the SS 430 were dissolved into the liquid brazing alloy forming Fe-Cr phases in the brazed seam.

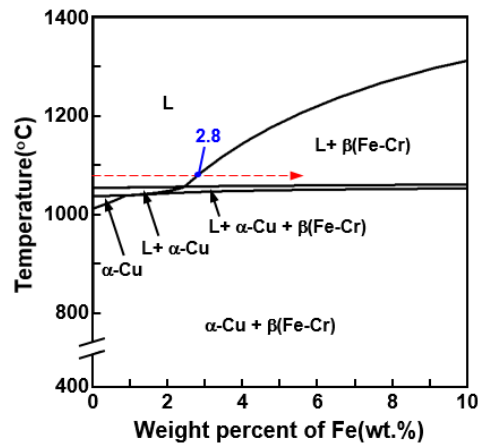


**Figure 13.** (Cu-6.4Al-0.6Cr)-xFe (wt%) quasi-binary phase diagram calculated via Thermo-calc software.

### 3.3.4. Relationship between the Microstructure and Hardness in the Brazed Seam

In order to approximately compare the plasticity of the brazed seams, the Vickers hardness was measured and averaged ( $n = 3$ ). Figure 14 shows the Vickers hardness of the brazed seam based on the composition of the brazing alloys and bonding temperature. The brazed seam with Cu-7Al-xTi alloys exhibited higher hardness than that with Cu-7Al-xZr alloys, and the hardness increased with increases in the Ti or Zr composition of the brazing alloys. Irrespective of the brazing alloys, the highest hardness was in the order of the 1000 °C seam, as-cast layer, and 1080 °C seam. It should be noted that when the hardness of the brazed seams was lower than 107 Hv, cracks were not observed in the brazed joint. This was potentially because a relatively brittle brazed seam could not relieve the residual stress, and thus the stress concentration caused the propagation of the crack in the joint [31,40].

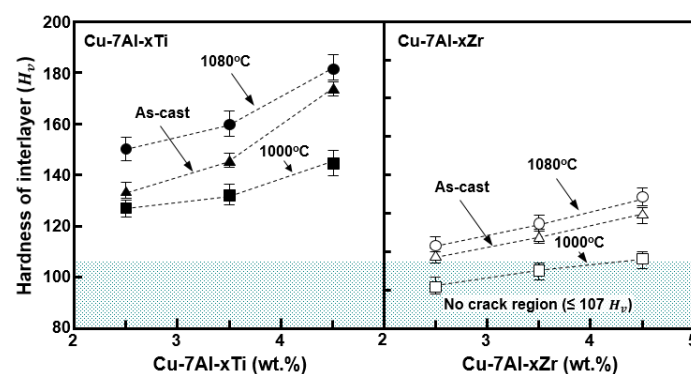


**Figure 14.** Hardness ( $H_v$ ) of the as-cast filler alloys, 1000 °C brazed seam, and 1080 °C brazed seam for the Cu-7Al-xTi and Cu-7Al-xZr ( $x = 2.5, 3.5, \text{ and } 4.5$ ) brazing alloys. The shaded area indicates that cracking did not occur under 107 Hv.

It was expected that the differences in hardness among the brazed seams were correlated with the fraction of the second phases formed in the brazed seam, and thus the nanoindentation hardness of each phase was measured via a nanoindenter (HM 200, Helmut Fischer, Sindelfingen, Germany). Nanoindentation was conducted with a 5 mN pressure for 10 s, and the hardness value was selected and averaged only since the indenter was pressed in the center of the phase. Measurement for hardness

using nanoindentation was duplicated at three different points in the brazed seam. Figure 15 shows representative SEM images of the nanoindentation hardness measurement of the  $\alpha$ -Cu matrix and the second phases in the brazed seam that were brazed at 1000 °C and 1080 °C by using Cu-7Al-3.5Ti and Cu-7Al-3.5Zr brazing alloys, respectively. Table 7 summarizes the nanoindentation hardness values for the  $\alpha$ -Cu matrixes and second phases. Here, AlCu<sub>2</sub>Ti and AlCu<sub>2</sub>Ti(Fe) were obtained after brazing at 1000 °C and 1080 °C, respectively, by using Cu-7Al-*x*Ti brazing alloys, and AlCu<sub>2</sub>Zr and Fe-Cr were the obtained phases brazed at 1000 °C and 1080 °C by using Cu-7Al-*x*Zr brazing alloys, respectively. The nanoindentation values of the  $\alpha$ -Cu matrix were in the range of 102–119 Hv irrespective of the bonding conditions. Conversely, the nanoindentation values of the second phases increased in the following order: Fe-Cr, AlCu<sub>2</sub>Zr, AlCu<sub>2</sub>Ti, and AlCu<sub>2</sub>Ti(Fe). It should be noted that the Fe-containing AlCu<sub>2</sub>Ti(Fe) phase exhibited the highest value of approximately 494 Hv, and this was 1.6 times that of the AlCu<sub>2</sub>Ti phase.

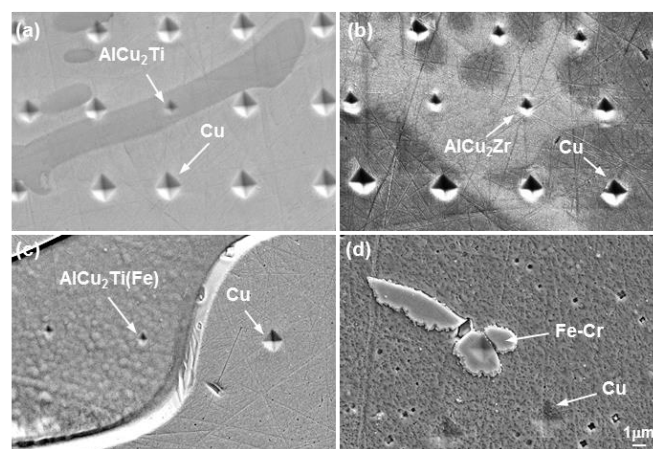


**Figure 15.** SEM images of the hardness evaluation of the phases in the brazed specimens: (a)  $\alpha$ -Al<sub>2</sub>O<sub>3</sub>/Cu-7Al-3.5Ti/SS 430 brazed at 1000 °C, (b)  $\alpha$ -Al<sub>2</sub>O<sub>3</sub>/Cu-7Al-3.5Zr/SS 430 brazed at 1000 °C, (c)  $\alpha$ -Al<sub>2</sub>O<sub>3</sub>/Cu-7Al-3.5Ti/SS 430 brazed at 1080 °C, and (d)  $\alpha$ -Al<sub>2</sub>O<sub>3</sub>/Cu-7Al-3.5Ti/SS 430 brazed at 1080 °C.

**Table 7.** Nanoindentation hardness of the phases in the brazed seam relative to brazing alloys and bonding temperature.

Brazing Alloy and Temperature	$\alpha$ -Cu	Second Phase
Cu-7Al- <i>x</i> Ti, at 1000 °C	112	297 (AlCu <sub>2</sub> Ti)
Cu-7Al- <i>x</i> Ti, at 1080 °C	119	494 (AlCu <sub>2</sub> Ti(Fe))
Cu-7Al- <i>x</i> Zr, at 1000 °C	104	260 (AlCu <sub>2</sub> Zr)
Cu-7Al- <i>x</i> Zr, at 1080 °C	102	231 (Fe-Cr)

Figure 16a shows the volume fraction of the second phases in the brazed seam based on the brazing alloys and bonding temperature, and the averaged value ( $n = 3$ ) from a cross-sectional area in the brazed seam were determined using the volume-area proportionality relation via Image Pro-Plus software (Media Cybernetics Inc., Rockville, MA, USA). The volume fractions of the Fe-Cr, AlCu<sub>2</sub>Zr, AlCu<sub>2</sub>Ti, and AlCu<sub>2</sub>Ti(Fe) phases were measured to be 20–25, 7.2–12.0, 12.3–19.0, and 20.0–25.0, respectively. When the Ti or Zr content increased under all conditions, the fraction of the second phases also increased.

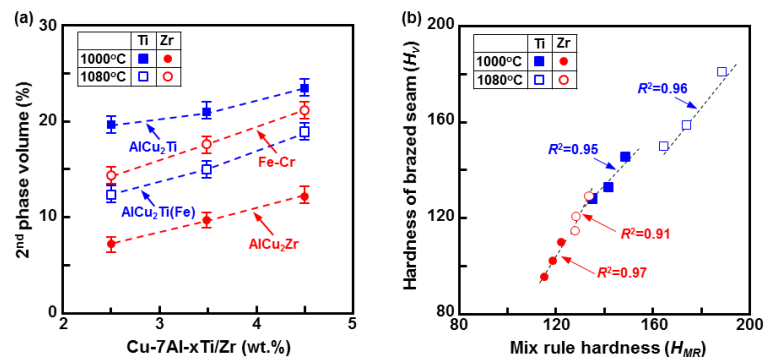


**Figure 16.** (a) Volume fraction of the second phases in the interlayer brazed with Cu-7Al-xTi/Zr ( $x = 2.5, 3.5,$  and  $4.5$ ) at  $1000\text{ }^{\circ}\text{C}$  and  $1080\text{ }^{\circ}\text{C}$ , and (b) relationships between the mix rule hardness and Vickers hardness for the brazed interlayer.

Generally, the hardness of a composite material including two materials is obtained based on the “mix rule”, and this is expressed as the sum of the product of the hardness and the fraction of each phase [41]. It is expected that the hardness of the brazed seam joint is obtained as follows:

$$H_{MR} = \sum H_i \times V_i \quad (1)$$

where  $H_{MR}$  denotes a total hardness of the mixed layer,  $H_i$  denotes the hardness of each phase and denotes the nanoindentation hardness in the study, and  $V_i$  denotes the fraction of each phases.

Figure 16b shows the correlation between the actual Vickers hardness ( $H_v$ ) and the mix-rule hardness ( $H_{MR}$ ) for each bonding condition, and this exhibited linear relationships based on the brazing alloy and bonding condition with an  $R^2$  value of 0.91–0.97. The Cu-7Al-xZr brazed joint at  $1000\text{ }^{\circ}\text{C}$  exhibited the lowest Vickers hardness without any cracks since AlCu<sub>2</sub>Zr intermetallic compounds with relatively lower nanoindentation hardness were distributed in small amounts. Therefore, it was concluded that the change in the hardness of the brazed seam was independent of the hardness and the fraction of the second phases formed in the brazed seam.

### 3.4. Relationship between the Residual Stress and Hardness of Bonded Interlayer

The residual stress measurements shown in Figure 4 and Table 4 were calculated by using physical and mechanical properties of the as-cast brazing alloys, although it did not reflect the mechanical property changes derived from the interfacial reaction between the brazing alloy and base metals (Al<sub>2</sub>O<sub>3</sub> and SS 430) during brazing. As shown in Section 3.1, cracks occurred at the brazed joint at  $1080\text{ }^{\circ}\text{C}$  with respect to the liquid state bonding with Cu-7Al-xZr brazing alloys albeit not at  $1000\text{ }^{\circ}\text{C}$  as the solid–liquid state bonding, although this was assumed to be caused by differences in the magnitude of the residual stresses based on the bonding temperature. Thus, even while using the same brazing alloy, the residual stress can be changed with respect to the bonding condition with different mechanical properties.

In order to acquire the maximum residual stress of the bonded specimens (which were already heat-treated during brazing), the mechanical properties, i.e., yield strength, of the brazed seam should be identified for the numerical calculation. However, the physical property value of the brazed seam layer of the  $200\text{ }\mu\text{m}$  thickness was excessively thin when measured, and thus it was postulated that the hardness of the brazed seam could be utilized to deduce the yield strength from their mechanical relationships to calculate the residual stress.

When intermediate layers, such as Cu, W, and Mo, are used in ceramic–metal bonding, the residual stress in the joints are considered to be dependent on the yield strength of the intermediate layer [26]. Therefore, the relationship between the measured yield strength (Table 2) of the as-cast brazing alloy and maximum residual stress (Table 4) was investigated, as shown in Figure 17a. The calculated maximum residual stress ( $\sigma_{max}$ ) linearly increased with respect to the yield strength ( $\sigma_y$ ) of the brazing

alloys. Although the number of data was low, the relationship between the yield strength of the brazing alloys and maximum residual stress ( $\sigma_{max}$ ) was linearly fitted with an  $R^2$  value of 0.96 and is expressed in Equation (2) as follows:

$$\sigma_{max} = 2.80\sigma_y + 276.0 \quad (2)$$

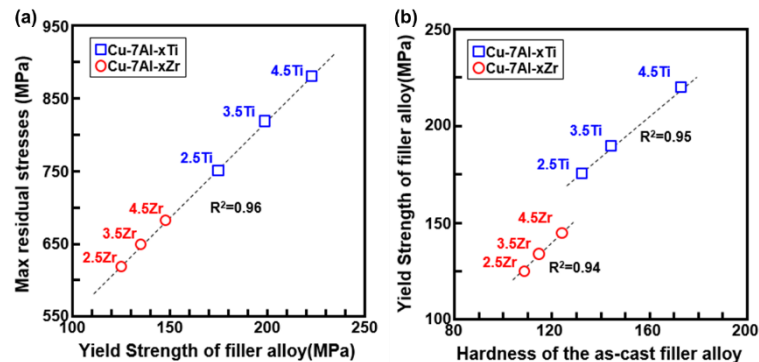


**Figure 17.** (a) Relationship between the yield strength ( $\sigma_y$ ) and max residual stresses ( $\sigma_{max}$ ) of the as-cast filler metals, and (b) relationships between the yield strength of each Cu-7Al-xTi ( $\sigma_{yT}$ ) and Cu-7Al-xZr ( $\sigma_{yZ}$ ) filler metals and hardness ( $H_v$ ) of the as-cast Cu-7Al-xTi ( $H_{vT}$ ) and Cu-7Al-xZr ( $H_{vZ}$ ) filler metals, respectively.

It was difficult to determine the yield strength of the 200  $\mu\text{m}$  brazed seam after brazing, and thus the yield strength was approximated using a Vickers hardness that is generally known to be proportional to the yield strength [42–44]. Figure 17b shows the relationships between the yield strength of each Cu-7Al-xTi ( $\sigma_{yT}$ ) and Cu-7Al-xZr ( $\sigma_{yZ}$ ) brazing alloys and Vickers hardness ( $H_v$ ) of the as-cast Cu-7Al-xTi ( $H_{vT}$ ) and Cu-7Al-xZr ( $H_{vZ}$ ) brazing alloys, respectively. As expected, the yield strength increased linearly with increased hardness. Their relationships linearly follow with  $R^2$  values of 0.94 and 0.95, respectively, and are expressed in Equations (3) and (4):

$$\sigma_{yT} = 1.26H_{vT} + 5.0 \quad (3)$$

$$\sigma_{yZ} = 1.10H_{vZ} + 7.1 \quad (4)$$

Based on their relationships, the yield strength and the maximum residual stress of the brazed seams after brazing were calculated via Equations (2)–(4) from the hardness of the brazed seams. The calculated results are shown in Table 8 and Figure 18. From the aforementioned results, it was inferred that when the hardness of the brazed seam was under 107 Hv, the yield strength was under 124 MPa or less, and the maximum residual stress generated in the  $\text{Al}_2\text{O}_3/\text{ABAs}/\text{SS 430}$  joint corresponded to 624 MPa or less, and thus we determined that the crack-free joint was obtained under that residual stress value.

**Table 8.** Calculated and max residual stresses ( $\sigma_{max}$ ) and yield strength ( $\sigma_y$ ) using the hardness ( $H_v$ ) of the brazed seams for Cu-7Al-xTi and Cu-7Al-xZr ( $x = 2.5, 3.5,$  and  $4.5$ ) brazing alloys via Equations (2)–(4).

Value	Bonding Temperature	Cu-7Al-xTi (wt%)			Cu-7Al-xZr (wt%)		
		2.5	3.5	4.5	2.5	3.5	4.5
$\sigma_{max}$	at 1000 °C	741	759	802	589	612	624
	at 1080 °C	819	851	932	644	668	699
$\sigma_y$	at 1000 °C	166	173	188	112	120	124
	at 1080 °C	194	205	234	131	140	151
$H_v$	at 1000 °C	128	133	145	95	103	107
	at 1080 °C	150	159	182	113	121	130

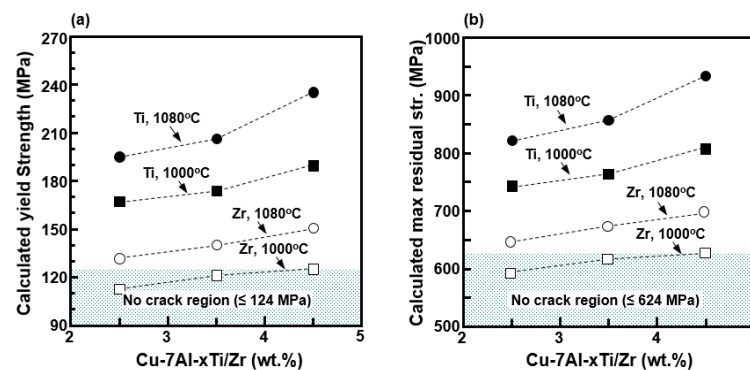


**Figure 18.** (a) Yield strength ( $\sigma_y$ ) and (b) max residual stress ( $\sigma_{max}$ ) calculated using Equations (2)–(4) with hardness ( $H_v$ ) of the 1000 °C and 1080 °C brazed interlayers for Cu-7Al-xTi and Cu-7Al-xZr filler metals ( $x = 2.5, 3.5,$  and  $4.5$ ). The shaded area denotes the absence of cracks under 124 MPa ( $\sigma_y$ ) and under 624 MPa ( $\sigma_{max}$ ).

#### 4. Conclusions

This study involved investigating the effect of bonding temperature on crack occurrences in  $\alpha$ -Al<sub>2</sub>O<sub>3</sub>/SS 430 joints using Cu-based active brazing alloys, i.e., Cu-7Al-xTi and Cu-7Al-xZr ( $x = 2.5, 3.5,$  and  $4.5$ ), and emphasized their microstructural characterization, hardness, and numerical residual stresses. The following conclusions were obtained:

- (1) The bonding temperature affected the crack occurrence in the joint. Cracks were observed in the joints brazed at 1080 °C irrespective of the brazing alloys, while crack-free joints were observed at 1000 °C with only Cu-7Al-xZr alloys.
- (2) The Cu-7Al-xTi and Cu-7Al-xZr brazed seams bonded at 1000 °C were composed of  $\alpha$ -Cu SS and eutectic ( $\alpha$ -Cu + AlCu<sub>2</sub>Ti and  $\alpha$ -Cu + AlCu<sub>2</sub>Zr, respectively) phases that were similar to those of their brazing alloys, thereby indicating that the partially liquefied brazing alloy in the solid-liquid state was conducted during the brazing process. Conversely, with increases in the brazing temperature to 1080 °C for liquid-state bonding, the brazed seam consisted of single phase AlCu<sub>2</sub>Ti(Fe) along  $\alpha$ -Cu SS and Fe-Cr phases in the  $\alpha$ -Cu matrix, and this indicated the dissolution of Fe from SS 430.
- (3) The hardness of the brazed seam at 1080 °C exceeded that of the brazed seam at 1000 °C, and the hardness of the Cu-7Al-xTi brazed seam exceeded that of the Cu-7Al-xZr brazed seam. A crack-free joint was obtained when the hardness of the brazed seam was under 107 Hv. The changes in Vickers hardness for different brazed joints corresponded to the sum of the product of the nanoindentation hardness and fraction of each phase.
- (4) Analytical and experimental approaches were integrated to calculate the maximum residual stresses of the real joint that was heat-treated during brazing. The yield strength of the brazing

alloys significantly affected the maximum residual stress of the joint and was dependent on the hardness of the brazing alloys. Based on their relationships, the maximum residual stresses of the real joint were obtained by using the yield strength and hardness of the brazed seams. When the hardness of the braze joint was less than 107 Hv, the yield strength was 124 MPa or less, thereby yielding a maximum residual stress corresponding to or less than 624 MPa. This aided in obtaining a crack-free joint.

**Author Contributions:** H.H., G.K., Y.-C.P., K.J., and C.-Y.K. conceived and designed the experiments; H.H. and G.K. performed the experiments; Y.-C.P., K.J., and C.-Y.K. analyzed the data; and H.H. wrote this paper.

**Funding:** This research was funded by a National Research Foundation of Korea (NRF) by the Korea government (MSIP) grant number (No. 2012R1A5A1048294).

**Conflicts of Interest:** The authors declare no conflict of interest. The funding sponsors had no role in the design of the study; in the collection, analyses, or interpretation of data; in the writing of the manuscript, or in the decision to publish the results.

## References

- Mizuhara, H.; Mally, K. Ceramic-to-metal joining with active brazing filler metal. *Weld. J.* **1985**, *64*, 27–32.
- Laik, A.; Mishra, P.; Bhanumurthy, K.; Kale, G.B.; Kashyap, B.P. Microstructural evolution during reactive brazing of alumina to inconel 600 using ag-based alloy. *Acta Mater.* **2013**, *61*, 126–138. [[CrossRef](#)]
- Ali, M.; Knowles, K.M.; Mallinson, P.M.; Fernie, J.A. Interfacial reactions between sapphire and Ag–Cu–Ti-based active braze alloys. *Acta Mater.* **2016**, *103*, 859–869. [[CrossRef](#)]
- Lee, D.; Woo, J.; Park, S. Oxidation behavior of Ag–Cu–Ti brazing alloys. *Mater. Sci. Eng. A* **1999**, *268*, 202–207. [[CrossRef](#)]
- Sudworth, J.; Tiley, A. *Sodium Sulphur Battery*; Springer Science & Business Media: Berlin, Germany, 1985.
- Heo, H.; Park, Y.-C.; Kang, C.-Y.; Jung, K. Dealloying of a Ag–Cu–Ti alloy in liquid sodium at 350 °C. *Corros. Sci.* **2018**, in press. [[CrossRef](#)]
- Jung, K.; Heo, H.-J.; Lee, J.-H.; Park, Y.-C.; Kang, C.-Y. Enhanced corrosion resistance of hypo-eutectic Al–1Mg–xSi alloys against molten sodium attack in high temperature sodium sulfur batteries. *Corros. Sci.* **2015**, *98*, 748–757. [[CrossRef](#)]
- Jung, K.; Lee, S.; Park, Y.-C.; Kim, C.-S. Finite element analysis study on the thermomechanical stability of thermal compression bonding (TCB) joints in tubular sodium sulfur cells. *J. Power Sour.* **2014**, *250*, 1–14. [[CrossRef](#)]
- Lu, X.; Li, G.; Kim, J.Y.; Mei, D.; Lemmon, J.P.; Sprenkle, V.L.; Liu, J. Liquid-metal electrode to enable ultra-low temperature sodium–beta alumina batteries for renewable energy storage. *Nat. Commun.* **2014**, *5*, 4578. [[CrossRef](#)] [[PubMed](#)]
- Min, J.K.; Lee, C.-H. Numerical study on the thermal management system of a molten sodium-sulfur battery module. *J. Power Sour.* **2012**, *210*, 101–109. [[CrossRef](#)]
- Singh, M.; Martinez Fernandez, J.; Asthana, R.; Rico, J.R. Interfacial characterization of silicon nitride/silicon nitride joints brazed using Cu-base active metal interlayers. *Ceram. Int.* **2012**, *38*, 2793–2802. [[CrossRef](#)]
- Heo, H.; Jung, K.; Kang, C.-Y. Development of Cu–Al–Ti Filler Metals for Al<sub>2</sub>O<sub>3</sub>/SS Brazed Joints Applied for Na-S Batteries Cells. In Proceedings of the 11th International Conference on Brazing, High temperature Brazing and Diffusion Bonding LOET, Aachen, Germany, 7 June 2016.
- Fernandez, J.M.; Asthana, R.; Singh, M.; Valera, F.M. Active metal brazing of silicon nitride ceramics using a Cu-based alloy and refractory metal interlayers. *Ceram. Int.* **2016**, *42*, 5447–5454. [[CrossRef](#)]
- Fan, D.; Huang, J.; Wang, Y.; Chen, S.; Zhao, X. Active brazing of carbon fiber reinforced SiC composite and 304 stainless steel with Ti–Zr–Be. *Mater. Sci. Eng. A* **2014**, *617*, 66–72. [[CrossRef](#)]
- Wu, Q.; Luo, Z.; Wang, Y.; Zhao, H.; Deng, Z. Effects of rare earth Ce on the brazing performance of high energy mechanical milling Cu-based alloy powder. *Metals* **2018**, *8*, 495. [[CrossRef](#)]
- Pelton, A. The Cu–Na (Copper–Sodium) system. *Bull. Alloy Ph. Diagr.* **1986**, *7*, 25–27. [[CrossRef](#)]
- Murray, J.L. The Al–Na (Aluminum–Sodium) system. *Bull. Alloy Ph. Diagr.* **1983**, *4*, 407–410. [[CrossRef](#)]
- Bale, C. The Na–Ti (Sodium–Titanium) system. *J. Ph. Equilibria* **1989**, *10*, 138–139. [[CrossRef](#)]
- Bale, C. The Na–Zr (Sodium–Zirconium) system. *J. Ph. Equilibria* **1987**, *8*, 50–51. [[CrossRef](#)]

20. Bobzin, K.; Öte, M.; Wiesner, S.; Kaletsch, A.; Broeckmann, C. Characterization of reactive air brazed ceramic/metal joints with unadapted thermal expansion behavior. *Adv. Eng. Mater.* **2014**, *16*, 1490–1497. [[CrossRef](#)]
21. Hattali, M.; Valette, S.; Ropital, F.; Mesrati, N.; Tréheux, D. Effect of thermal residual stresses on the strength for both alumina/Ni/alumina and alumina/Ni/nickel alloy bimetals. *J. Mater. Sci.* **2009**, *44*, 3198–3210. [[CrossRef](#)]
22. Iancu, O.T.; Munz, D.; Eigenmann, B.; Scholtes, B.; Macherauch, E. Residual stress state of brazed ceramic/metal compounds, determined by analytical methods and X-ray residual stress measurements. *J. Am. Ceram. Soc.* **1990**, *73*, 1144–1149. [[CrossRef](#)]
23. Levy, A. Thermal residual stresses in ceramic-to-metal brazed joints. *J. Am. Ceram. Soc.* **1991**, *74*, 2141–2147. [[CrossRef](#)]
24. Nakao, Y.; Nishimoto, K.; Saida, K.; Nakamura, H.; Katada, K. Fundamental study on  $\text{Si}_3\text{N}_4$  metal bonding using Cu-base alloy as the insert metal. *Q. J. Jpn. Weld. Soc.* **1989**, *7*, 136–142. [[CrossRef](#)]
25. Zhou, Y.; Ikeuchi, K.; North, T.H.; Wang, Z. Effect of plastic deformation on residual stresses in ceramic/metal interfaces. *Metall. Trans. A* **1991**, *22*, 2822–2825. [[CrossRef](#)]
26. Zhou, Y.; Bao, F.; Ren, J.; North, T. Interlayer selection and thermal stresses in brazed  $\text{Si}_3\text{N}_4$  steel joints. *Mater. Sci. Technol.* **1991**, *7*, 863–868. [[CrossRef](#)]
27. Blugan, G.; Kuebler, J.; Bissig, V.; Janczak-Rusch, J. Brazing of silicon nitride ceramic composite to steel using SiC-particle-reinforced active brazing alloy. *Ceram. Int.* **2007**, *33*, 1033–1039. [[CrossRef](#)]
28. Jacobson, D.M.; Humpston, G. *Principles of Brazing*; ASM International: Russell Township, OH, USA, 2005.
29. Nakao, Y.; Nishimoto, K.; Saida, K. Reaction layer formation in nitride ceramics ( $\text{Si}_3\text{N}_4$  and AlN) to metal joints bonded with active filler metals. *ISIJ Int.* **1990**, *30*, 1142–1150. [[CrossRef](#)]
30. Korojy, B.; Ekbohm, L.; Fredriksson, H. On solidification shrinkage of copper-lead and copper-tin-lead alloys. *Int. J. Cast Met. Res.* **2009**, *22*, 179–182. [[CrossRef](#)]
31. Xu, C.; Xiao, G.; Zhang, Y.; Fang, B. Finite element design and fabrication of  $\text{Al}_2\text{O}_3/\text{TIC}/\text{CaF}_2$  gradient self-lubricating ceramic tool material. *Ceram. Int.* **2014**, *40*, 10971–10983. [[CrossRef](#)]
32. Xu, Y.; Jung, K.; Park, Y.-C.; Kim, C.-S. Selection of container materials for modern planar sodium sulfur (NaS) energy storage cells towards higher thermo-mechanical stability. *J. Energy Storage* **2017**, *12*, 215–225. [[CrossRef](#)]
33. ASTM International. *Astm E8/E8m-09 Standard Test Methods for Tension Testing of Metallic Materials*; ASTM International: West Conshohocken, PA, USA, 2011.
34. Davis, J.R. *Copper and Copper Alloys*; ASM International: West Conshohocken, PA, USA, 2001.
35. Boyer, H.E. *Atlas of Stress-Strain Curves*; ASM International: Metals Park, OH, USA, 1987.
36. Fernie, J.A.; Drew, R.A.L.; Knowles, K.M. Joining of engineering ceramics. *Int. Mater. Rev.* **2013**, *54*, 283–331. [[CrossRef](#)]
37. Singh, A.; Tang, L.; Dao, M.; Lu, L.; Suresh, S. Fracture toughness and fatigue crack growth characteristics of nanotwinned copper. *Acta Mater.* **2011**, *59*, 2437–2446. [[CrossRef](#)]
38. Zuo, X.; Guo, R.; Zhao, C.; Zhang, L.; Wang, E.; Han, K. Microstructure and properties of Cu-6wt% Ag composite thermomechanical-processed after directionally solidifying with magnetic field. *J. Alloys Compd.* **2016**, *676*, 46–53. [[CrossRef](#)]
39. Kim, M.-B.; Kim, S.-J.; Lee, B.-K.; Yuan, X.; Yoon, B.-H.; Woo, I.-S.; Kang, C.-Y. Effect of the heat input on the tensile properties in arc brazing of ferritic stainless steel using Cu-Si insert alloy. *Korean J. Met. Mater.* **2010**, *48*, 289–296. [[CrossRef](#)]
40. Shi, J.M.; Zhang, L.X.; Pan, X.Y.; Tian, X.Y.; Feng, J.C. Microstructure evolution and mechanical property of ZrC-SiC/Ti6Al4V joints brazed using Ti-15Cu-15Ni filler. *J. Eur. Ceram. Soc.* **2018**, *38*, 1237–1245. [[CrossRef](#)]
41. Kim, H.S. On the rule of mixtures for the hardness of particle reinforced composites. *Mater. Sci. Eng. A* **2000**, *289*, 30–33. [[CrossRef](#)]
42. Kong, J.P.; Kang, C.Y. Effect of alloying elements on expulsion in electric resistance spot welding of advanced high strength steels. *Sci. Technol. Weld. Join.* **2016**, *21*, 32–42. [[CrossRef](#)]

43. Busby, J.T.; Hash, M.C.; Was, G.S. The relationship between hardness and yield stress in irradiated austenitic and ferritic steels. *J. Nucl. Mater.* **2005**, *336*, 267–278. [[CrossRef](#)]
44. Pavlina, E.J.; Van Tyne, C.J. Correlation of yield strength and tensile strength with hardness for steels. *J. Mater. Eng. Perform.* **2008**, *17*, 888–893. [[CrossRef](#)]



© 2018 by the authors. Licensee MDPI, Basel, Switzerland. This article is an open access article distributed under the terms and conditions of the Creative Commons Attribution (CC BY) license (<http://creativecommons.org/licenses/by/4.0/>).